

An injection seeded narrow bandwidth pulsed optical parametric oscillator and its application to the investigation of hyperfine structure in the PF radical

James A. J. Fitzpatrick, Oleg V. Chekhlov,^{a)} John M. F. Elks, and Colin M. Western^{b)}
School of Chemistry, University of Bristol, Cantock's Close, Bristol BS8 1TS, United Kingdom

Stephen H. Ashworth
School of Chemical Sciences, University of East Anglia, Norwich NR4 7TJ, United Kingdom

(Received 27 June 2001; accepted 31 July 2001)

We describe the construction of an all solid-state, narrow bandwidth, pulsed optical parametric oscillator (OPO) based on β -barium borate nonlinear crystals. The OPO was injection seeded by an external cavity diode laser in the range 755–855 nm to generate high power narrow bandwidth tunable light in this range and simultaneously at 606–669 nm. The bandwidth of the visible light was ~ 130 MHz, and after frequency doubling or sum frequency mixing with the second harmonic of the pump Nd:YAG laser, sub-Doppler spectra with an overall resolution of 450 MHz were taken in the UV. The system is demonstrated by taking high-resolution spectra of the $v' = 2-3$ and $5-7$ bands of the $A^3\Pi-X^3\Sigma^-(v',0)$ progression and the $v' = 4-v'' = 0$ band of the $d^1\Pi-a^1\Delta$ transition in PF. These spectra show clear hyperfine structure, and an analysis of this structure is presented and interpreted in terms of the electronic structure of the molecule. As a prelude to this high-resolution study, the first ten members of the $A-X$ band system and the first five members of the $d-a$ band system were recorded at the moderate resolution provided by a pulsed dye laser. © 2001 American Institute of Physics. [DOI: 10.1063/1.1405121]

I. INTRODUCTION

The use of optical parametric oscillators (OPO) has become increasingly popular in the last decade in molecular spectroscopy, photochemistry, and many other areas. In addition to the well recognized advantages of the OPO as an all solid-state design, the possibility of broad tunability especially in the infrared and high peak powers makes them an excellent source of coherent light for spectroscopy at convenient resolutions (~ 0.1 cm⁻¹). The spectra that can be obtained at this resolution contain a wealth of information about the motions of, and interactions between, the electrons and nuclei within the molecule of interest. Higher resolution would benefit many applications, and some completely new areas are opened up. For example, at the highest level of spectral resolution, hyperfine splittings due to the different orientations of the nuclear spins become visible. The constants describing these splittings can yield direct information on the electronic wave function such as the amount of s character or spin density at each nucleus. See, for example, a previous detailed study on the A state of iodine monochloride^{1,2} where the electronic wave function was probed over a large range of internuclear distance by measuring hyperfine splittings over a wide range of vibrational levels. Other applications requiring high-resolution are the electronic spectra of large molecules³ and photodissociation dynamics.⁴

Previously, the only way to obtain the resolution required in these cases was to use continuous wave (cw) dye lasers, or other even more specialist techniques. While cw systems have very low bandwidths (~ 1 MHz) they can be difficult to operate, and the peak powers are low. The latter makes the nonlinear optical techniques (such as second harmonic generation) that have become essential in modern spectroscopy inconvenient to implement. A system that combines the resolution attainable from a cw laser with the high peak powers and ease of operation of a pulsed laser system is obviously desirable. This has been achieved previously by amplifying a cw dye laser with a pulsed system (see, for example, Ref. 4). Such a system may attain the resolution and peak powers required but, given that a cw dye laser is required, it is difficult and expensive to operate. An approach that has become feasible recently is to amplify diode lasers, which are very easy to operate, with an OPO. This paper describes such a system, and its application to the sub-Doppler spectroscopy of two electronic transitions in the PF radical. The hyperfine structure revealed in these transitions is analyzed in terms of the bonding in PF. A preliminary report of this work, covering a single vibrational level of the $A^3\Pi$ state, has already appeared.⁵

The possibility of single frequency OPO generation has been known since the early work of Bjorkholm and Danielmeyer.⁶ They demonstrated injection seeding of a lithium niobate (LiNbO₃) based OPO system. The OPO was pumped by a ruby laser and was seeded with a cw Nd:YAG laser. The cavity was locked to the seed light via a piezo-mounted end mirror and servo loop circuitry. Without seeding, the output from their OPO was highly multi-mode, but

^{a)}Permanent address: Institute of Physics, National Academy of Sciences of Belarus, Minsk, Belarus.

^{b)}Electronic-mail: c.m.western@bris.ac.uk

with seeding oscillation on a single longitudinal mode was observed. More recently, methods other than injection seeding for single frequency operation of the OPO have been demonstrated. These include the use of intra-cavity spectral elements in the resonator such as an intra-cavity étalon⁷ or simple amplification (without using a cavity) of an external narrow bandwidth laser source in a series of nonlinear crystals.⁸ The development of effective nonlinear optical materials such as BBO (β -barium borate), KTP/KTA (potassium titanyl phosphate/arsenate) and periodically poled materials (e.g., *pp*-LiNbO₃) has also led to further investigations into injection seeding. One of the prominent features of OPO systems is the oscillation simultaneously at two different frequencies (signal and idler) so injection seeding on just one of those frequencies leads to single mode oscillation of both outputs. Up until recently, injection seeding of BBO based OPO systems has been achieved at the signal wave, with the seed provided by a Nd:YAG,⁹ or a pulsed^{10,11} or a single frequency dye laser.¹² However, applicability of such systems to narrow bandwidth work has been limited because of the complexity and expense of cw dye lasers.

Fortunately, in recent years, a number of commercial external cavity cw diode lasers have become available which provide good coverage of the spectral range usually associated with the idler frequency of a UV pumped OPO system. These diode lasers are more attractive as single frequency seed sources than cw dye lasers due to their compactness, easy operation and substantially lower cost, and have already been demonstrated as effective cw seed sources for LiNbO₃,^{13,14} and BBO based systems.¹⁵ Application of these single frequency cw diode lasers for injection seeding OPO systems at the idler frequency provides an excellent route to obtain single frequency operation at the higher frequency signal wave in the visible region of the spectrum. When combined with relatively simple frequency doubling and mixing schemes, most of the spectral range from the near infrared to the UV can be covered at near transform limited bandwidth.

As an application of this narrow bandwidth light source, we have undertaken a high resolution study of the overlapping $A^3\Pi-X^3\Sigma^-$ and $d^1\Pi-a^1\Delta$ band systems in PF, where our resolution in the UV is sufficient to resolve the hyperfine structure in both band systems. PF is a rewarding candidate for the measurement of hyperfine structure as it has two spin $\frac{1}{2}$ nuclei, both with relatively large magnetic moments, which implies easily resolvable hyperfine splittings. Approximate potential energy curves for the low lying bound states of PF are shown in Fig. 1.

The $A^3\Pi-X^3\Sigma^-$ system in PF was first investigated by Douglas and Frackowiak¹⁶ who observed rotationally resolved emission from $v'=0, 1$ and 2 in the $A^3\Pi$ state to a range of ground state vibrational levels. It was observed that the vibrational structure of the A state is anomalous, with the vibrational spacings increasing with increasing v . All three spin-orbit components were identified with a splitting of $\sim 140\text{ cm}^{-1}$ and the Λ -doublet splitting between the $\Omega=0^+$ and $\Omega=0^-$ parities increased from 0.07 cm^{-1} for $v=0$ to 0.25 cm^{-1} for $v=2$. A more detailed analysis was undertaken by Kovács¹⁷ who utilized both spin-orbit and ef-

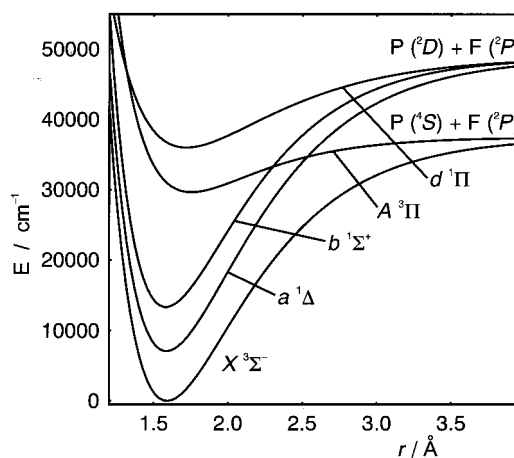


FIG. 1. Schematic potential energy curves for electronic states correlating to the first and second atomic asymptotes in the PF radical.

fective spin-spin parameters to produce a more accurate description of Douglas and Frackowiak's data. Additional low-resolution data for the $A^3\Pi$ state were presented by Roychowdhury *et al.*¹⁸ in the form of a selection of spin-orbit sub-band head positions for $v'=0-9$ identified in emission at a resolution of 4.5 cm^{-1} . This study also made measurements of relative emission intensities for $v'=0-3$; the deviations of these from the Franck-Condon predictions are sufficient to suggest a strong r dependence to the transition moment as in the corresponding $A-X$ transition in the isoelectronic SO radical.¹⁹ These deviations have since been confirmed in a paper by Setser and co-workers²⁰ in which they determined radiative lifetimes for $v=0$ and 1 of the A state of $4.2 \pm 0.2\ \mu\text{s}$ and $3.2 \pm 0.2\ \mu\text{s}$, respectively. Further radiative lifetimes were reported by Nizamov and Setser²¹ as the current study was being undertaken; this paper also extended the rotational analysis to a wider range of vibrational levels of the A state.

Also relevant to the current work are the rotational and magnetic hyperfine constants measured for $v=0$ in the $X^3\Sigma^-$ ground state by Saito *et al.*²² using microwave spectroscopy. They were able to determine Fermi contact and nuclear spin-electron spin constants for both nuclei, which allowed them to derive values for the spin density and the s character of the wave function at each nucleus. Recent *ab initio* calculations by de Brouckère^{23,24} at the configuration interaction (CI) level have yielded hyperfine parameters that are in moderate agreement with the ground state hyperfine constants measured by Saito *et al.*,²² although the calculations were limited to the nuclear spin-spin constants and the quadrupole coupling constant for ^{17}F at the equilibrium geometry.

Douglas and Frackowiak¹⁶ also reported the first observations of a number of singlet states, namely the $a^1\Delta$, $b^1\Sigma^+$, $d^1\Pi$ and $g^1\Pi$ states, as illustrated in Fig. 1. Rotationally resolved spectra for both the $d-a$ and $d-b$ systems were recorded and analyzed for levels up to $v'=3$ in the $d^1\Pi$ state. Based on the fact that the d state vibrational spacing showed similar behavior to that of the A state, it was proposed that they had the same electronic configuration.

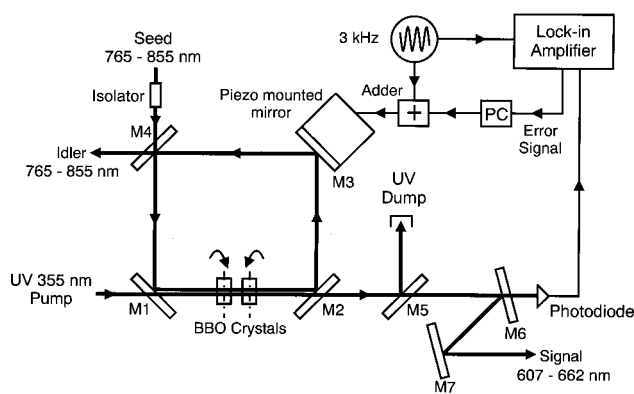


FIG. 2. Schematic of the OPO cavity and locking control system. The ring cavity is formed by four plane mirrors (M1–M4) which only reflect the idler wavelengths. Active cavity length control is provided by a piezo-mounted mirror (M3) and computer (PC) controlled servo loop electronics which include a photodiode, lock-in amplifier and a signal combiner (adder). The UV pump beam is introduced through mirror M1 and is separated from the signal beam by an additional dichroic mirror (M5) after exiting the cavity. Arrows by the BBO crystals indicate their contra-rotation about the axes shown in the diagram.

This is consistent with the relative emission intensities reported by Setser and co-workers²⁰ for the d - a and d - b band systems which seem to indicate again that the Franck–Condon factors do not provide an adequate explanation of experimental observations. In the case of the d state, however, no vibrational dependence of radiative lifetime was identified. The relative positioning of the singlet and triplet manifolds was established by Colin *et al.*²⁵ who observed the spin forbidden $b^1\Sigma^+ - X^3\Sigma^-$ transition.

Ab initio studies performed at the CI level by Latifzadeh and Balasubramanian²⁶ yielded potential curves for all of the electronic states correlating to the first two dissociation asymptotes. These confirm that all of the bound valence states had been identified experimentally by Douglas and Frackowiak.¹⁶ The $g^1\Pi$ state they observed has been assigned as the first member of the $[PF^+ 2\Pi](n\sigma)$ Rydberg series.^{16,27}

The format of the paper is as follows. Section II describes the construction of the injection seeded OPO system including the mechanism to lock the cavity length, and the performance of the system. Section III presents our low-resolution spectra and analysis of both the A - X band system and the d - a band system, which overlaps the A - X system. Sections IV and V detail our high-resolution investigation of the same systems with the injection seeded OPO system and in Sec. VI we discuss the bonding in PF as revealed by the hyperfine parameters.

II. EXPERIMENT

A. OPO cavity design

The OPO system (as illustrated in Fig. 2) is based on two BBO nonlinear optical crystals inserted in a singly resonant ring cavity. Both BBO crystals were $8 \times 12 \times 13$ mm and were cut to a phase matching angle of $\sim 28.0^\circ$ corresponding to a type I phase matching parametric process for the 355 nm pump wavelength. The surfaces of both crystals had a broad-

band visible anti-reflection coating. The crystals were mounted in a walk off compensation geometry as described by Bosenberg *et al.*²⁸ The optical axes of the crystals were constrained to equal and opposite angles in a counter-rotating mount. A dc motor provided high precision rotation of both crystals and additional fine-tuning was possible by adjustment of the voltage to a piezo-mount driving the same motion.

Four flat dichroic mirrors define the OPO cavity (see Fig. 2), which by choice of the mirror reflectivities and servo loop feedback is resonant with the idler frequency. The ring configuration provides ease of alignment, unidirectional output, and optical isolation of the potentially damaging (to the seed laser) high power light circulating in the OPO cavity. The length of the resonator was 21 cm, which corresponds to a cavity round trip time of 0.7 ns. The UV pump pulse length is 10 ns, which corresponds to 14 optical round trips while the pump field is present in the crystals. The output coupler (mirror M4) has $R \sim 85\%$ for the idler frequency, while the other cavity mirrors (M1–M3) have $R > 99\%$ for the idler frequency (in this case a spectral window of 750–880 nm). All four of the cavity mirrors are coated to enable high transmission of the signal and pump frequencies to prevent any doubly resonant behavior and any possible mode competition between the signal and idler outputs.

The OPO was pumped by the third harmonic of a Spectra Physics Quanta Ray Pro 190 injection seeded, single frequency Nd:YAG laser. This system provided a pulse length of 10 ns at 355 nm, which is longer than normal for this type of system to aid in minimizing the bandwidth of the OPO outputs. The available UV pump power was 220 mJ per pulse. The crystals were typically pumped with a fraction of the available power (~ 60 mJ per pulse) because the output power required from the OPO system for this study was quite small (1–2 mJ per pulse on the signal wave). The size of the pump beam was 8 mm in diameter, and the beam profile was close to Gaussian with $< 20\%$ modulation at the peak. No special efforts were made to smooth the beam shape. The spectral width of the pump laser was measured at 532 nm with a scanned Fabry–Perot interferometer and was determined to be 85 MHz (0.0028 cm^{-1}). The pump pulse was introduced into the cavity by transmission through mirror M1 and was separated from the signal wave by an additional dichroic mirror outside of the cavity after mirror M2.

The OPO resonator was seeded by a commercial single frequency external cavity diode laser (EOSI 2010) in the Littman configuration. This system generated narrow bandwidth (~ 5 MHz long term) light, and in the current study two different diode modules covered the spectral range 765–795 and 825–855 nm. The coarse tuning range of each diode module is typically 20–30 nm with a mode-hop free tuning range of ~ 40 GHz provided by a piezo element. Typical power outputs from the seed laser are of the order of a few mW. The output of the OPO was insensitive to the power of the seed laser. This is consistent with the other injection seeded OPO systems,^{13,15,29} where seed energies¹⁵ down to 300 μW have been sufficient to achieve single mode output.

B. Cavity locking system

To achieve single frequency OPO operation with injection seeding of cw laser radiation, the cavity length must be adjusted so that one of the cavity modes is resonant with the injected radiation. This mode is then excited by the low power external radiation. This resonant condition must be maintained while the seed laser is scanned. (Note that as single mode scan range is limited to ~ 40 GHz by the seed laser the BBO crystal angle can be held fixed during a scan.) The OPO cavity length was locked to the cw diode laser by monitoring the light transmitted through the cavity and maintaining the transmission at a maximum. This was achieved by modulating the cavity length by applying a low amplitude 3 kHz sine wave to the piezo-mounted mirror M3. The modulation this induced of the transmission of the cw diode laser through the OPO cavity was detected by a silicon photodiode (PD), which was situated after mirror M6 and a filter to block the signal radiation. The modulated signal from the photodiode was demodulated using a precision lock in amplifier (EG&G Brookdeal 9503). The phase sensitive output was used as the error signal, input to a PC, for cavity length control. Including a PC with an ADC/DAC in our cavity length control loop proved very beneficial; analogue electronics can maintain a fixed cavity length for a purely cw system fairly easily, but tuneable pulsed systems introduce complications that require careful handling using a purely analogue system. The first complication is the high light intensity while the pump pulse is present, which saturates the detectors and produces a large glitch in the error signal. This is easily handled by receiving a trigger signal from the pump laser and freezing the feedback process until the error signal has stabilized after the pulse. The other complication is the limited scan range of the cavity length control piezo (~ 6 GHz) requiring regular jumps to a different cavity mode. This requires that the mirror be rapidly moved to the opposite end of the range when it reaches one of its limits. This can be synchronized with the pump pulse to minimize disruption.

The locking algorithm used is straightforward in the absence of the above special cases. The computer response was designed to be similar to an analogue proportional-integral-derivative (PID) control. The mechanical and electronic constraints on the system are such that there were no problems with the frequency response of the computerized feedback. The biggest advantage of this approach was the ease of implementation and adjustment of the feedback parameters. An alignment mode was also programmed where the cavity length is continuously scanned to allow the alignment of the cavity to be optimized.

C. OPO performance

Ideally the injection seeding of the OPO system should narrow the bandwidth of the signal and idler output frequencies from a free running bandwidth of >1 cm^{-1} to a Fourier transform limited bandwidth. For a pulse with a Gaussian temporal profile $\Delta\nu_{\text{FWHM}}\Delta\tau_{\text{FWHM}}=0.44$, so for our 10 ns pump pulse, $\Delta\nu_{\text{FWHM}}=44$ MHz (0.0014 cm^{-1}). In practice the pulse will not have a Gaussian profile, and the OPO

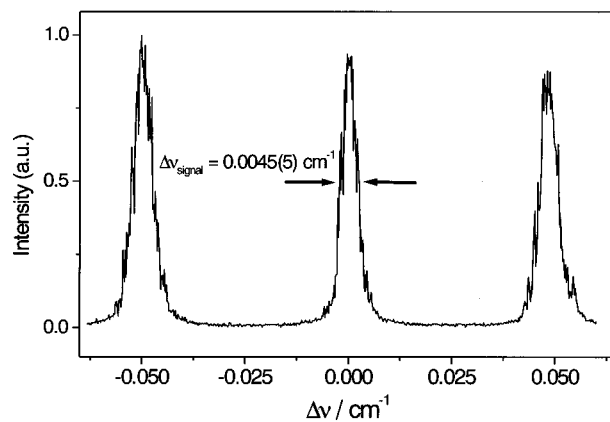


FIG. 3. Transmission fringes of the signal wave output from the injection seeded OPO system through a high finesse Fabry-Perot étalon.

outputs will have pulse lengths shorter than the 10 ns pump pulse. The linewidth actually achieved is demonstrated quite clearly in the spectrum of the signal wave (Fig. 3), which was taken using a high finesse Fabry-Perot interferometer while the seed frequency was scanned. The experimentally determined linewidth in the frequency domain has a FWHM of 130 ± 30 MHz with what appears to be a Gaussian line shape. Note that these traces represent several hundred OPO pulses and the single shot linewidth may be narrower.

In the time domain, the signal wave pulses exhibit a pulse width of 6.5 ± 0.5 ns. Using this pulse duration with the relation $\Delta\nu_{\text{FWHM}}\Delta\tau_{\text{FWHM}}=0.44$, the Fourier transform limit is predicted to be 68 ± 6 MHz. The measured bandwidth is thus only twice the transform limit for a Gaussian pulse. These measurements were performed at a pump energy of ~ 60 mJ per pulse, providing 6 mJ in the signal wave with 35 mJ remaining in the pump wave. Preliminary studies with a longer cavity length of 40 cm found a higher threshold and a slight shortening of the pulse duration of both the signal and idler waves but with no obvious change to the linewidth of the signal wave.

The only limitation to tunability in the current design is the mirrors M1-M3 which must reflect only the idler. At some idler wavelengths it is not possible to make mirrors that will not also reflect at 355 nm, requiring a separate mirror to combine the beams, as, for example, in Ref. 12. Such a design would require some lengthening of the cavity but, as mentioned above, this does not degrade the performance of the system. With this modification, the availability of tuneable diode lasers between 650 and 1500 nm means that the OPO system, when combined with frequency doubling or mixing, gives good coverage down to 200 nm.

D. Spectra

A pulsed supersonic jet expansion of PF radicals was generated by applying an electric discharge³⁰ to a mixture of 4% PF_3 in argon, at a backing pressure of 1 atm, prior to its expansion through a pinhole into a high vacuum chamber. Fluorescence excited using an unfocused laser beam was imaged onto a photomultiplier tube (PMT). For the highest resolution studies, the Doppler broadening was minimized

by selecting the central part of the image of the gas expansion with a slit in front of the PMT as in a similar study on ICl (see Ref. 31). Fluorescence signals were recorded with a PC using a digitizing oscilloscope (100 MHz sampling rate) for boxcar averaging. The low resolution study was performed using a Spectron Nd:YAG 532 nm pumped Spectra Physics PDL-3 dye laser with a linewidth of $\sim 0.1 \text{ cm}^{-1}$. All of the high-resolution work was performed using the new injection seeded OPO system. The absolute frequency was determined with a commercial wavemeter (Cluster LM-007) to an accuracy of 0.03 cm^{-1} for the fundamental output of the pulsed dye laser and 0.003 cm^{-1} for the frequency of the seed light. The absolute band positions from the high-resolution study given below are, however, not this accurate because they also depend on the frequency of the Nd:YAG pump laser. There could also be a systematic Doppler shift if the center of the gas expansion was not imaged. Neither of these factors would affect the dispersion of the recorded spectra, but there is a possible systematic error in the band origins; we estimate this to be up to 0.05 cm^{-1} .

III. RESULTS

Low-resolution spectra were recorded in the frequency range $28\,500\text{--}33\,600 \text{ cm}^{-1}$. Two overlapping electronic band systems were observed, which could be assigned to the $A^3\Pi-X^3\Sigma^-$ and $d^1\Pi-a^1\Delta$ transitions. Based on the relative intensities, it appears that significant population of the metastable $a^1\Delta$ state was achieved during the electric discharge.

A. The A–X band system

The strong $A-X(v',0)$ progression was dominant in the region investigated; transitions from $v'=0\text{--}9$ were observed with the fluorescence intensity decreasing with increasing v' . Several weak ($v',1$) hot bands were also identified. Assignment of the vibronic features was relatively simple as a result of the spin-orbit sub-band head positions reported by Roychowdhury *et al.*¹⁸ A spectrum of the $A^3\Pi_0-X^3\Sigma^-(0,0)$ sub-band is shown in Fig. 4.

The rotational and fine structure of each band was analyzed using a Hamiltonian of the form

$$\begin{aligned} \hat{H} = & B\hat{N}^2 - D\hat{N}^4 + A\hat{L}\cdot\hat{S} + \frac{2}{3}\lambda(3\hat{S}_z^2 - \hat{S}^2) \\ & + \frac{1}{2}\lambda_D[\frac{2}{3}(3\hat{S}_z^2 - \hat{S}^2), \hat{N}^2]_+ \\ & + \frac{1}{2}o(\hat{S}_+^2 e^{-2i\phi} + \hat{S}_-^2 e^{+2i\phi}) + \gamma\hat{N}\cdot\hat{S}. \end{aligned} \quad (1)$$

The upper state band origins and molecular constants arising from fitting the rotational line positions to the above Hamiltonian are given in Table I. All of the observed transitions fitted to within the experimental accuracy. For $v'=0\text{--}8$ it was possible to include transitions to all three of the spin-orbit components, making use of hot bands where required due to nonoverlapping dye ranges. In the weak (9,0) band only the strongest transitions to rotational levels in the central spin-orbit component were included in the fit. Transitions to $\Omega'=0$ and 2 were observed at the expected frequencies but with very poor signal-to-noise ratio.

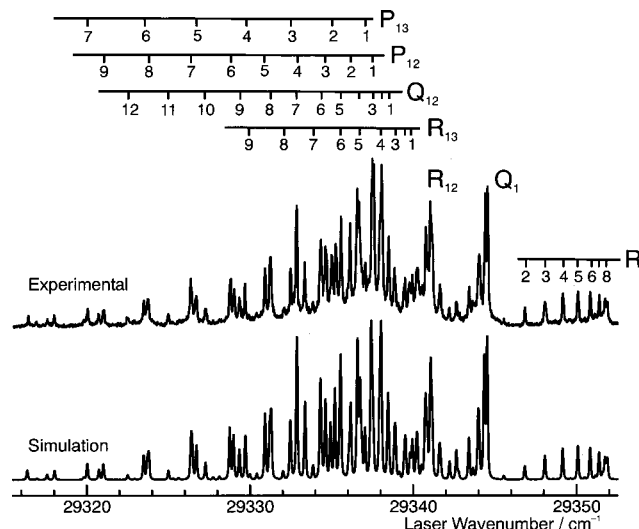


FIG. 4. A rotationally resolved spectrum of the $A^3\Pi_0-X^3\Sigma^-(0,0)$ band of the PF radical. The upper trace shows experimental data and the lower trace is a simulation generated from the constants given in Table I. The combs above the spectrum are labeled by lower state J . The linewidth of the simulation is a Voigt profile with a Gaussian component of 0.08 cm^{-1} and a Lorentzian component of 0.03 cm^{-1} .

The lower state constants were held fixed at the values determined by Saito *et al.*²² ($v''=0$) and Yamada *et al.*³² ($v''=1$) from microwave and infrared spectroscopy, respectively. It should be noted that corrections to the ground state rotational constants were made for both $v''=0$ and 1. For the microwave data ($v''=0$) a small correction to B was required to reproduce the published line list. The magnitude of the change, from $16\,920.976\,3(47) \text{ MHz}$ to $16\,921.014\,3(25) \text{ MHz}$ is of the order of D or λ_D and is either a typographical error or a difference in how the centrifugal distortion terms are expressed. The difference in the values, $1.3 \times 10^{-6} \text{ cm}^{-1}$, is sufficiently small that its effect on the low J lines investigated here is of no importance. A typographical error appears to be responsible for the $v''=1B$ constant of Yamada *et al.*³² being given as $0.599\,783\,6(70) \text{ cm}^{-1}$ instead of the value $0.559\,783\,6(70) \text{ cm}^{-1}$ suggested by refitting their line list. This correction obviously has a much larger effect which is perceptible even in the low-resolution ($v',1$) spectra.

The constants given in Table I are in excellent agreement with the recent values given by Nizamov and Setser.²¹ Note that they use a different definition for two of the fine structure constants, as they interpret their values in terms of interactions with different electronic states. The resulting Hamiltonian is identical provided the replacements $\beta = -2\lambda$ and $O = -2o$ are made. Consistent with their results neither our low-resolution data nor the high-resolution data presented below showed a J dependence to the lambda doubling. Their measurements are potentially more sensitive to this as their rotational temperature (300 K) was much higher than in our gas expansion. For the same reason they were able to make a better determination of the centrifugal distortion constant, D and the spin rotation constant, γ .

Our measurements have extended the range of rotationally analyzed A state levels up to $v'=9$. This provided the

TABLE I. Rotational and fine structure constants for the $A^3\Pi$ state of PF.^a

v'	Origin/cm ⁻¹	B /cm ⁻¹	A /cm ⁻¹	λ /cm ⁻¹	o /cm ⁻¹
0	29 481.7578(40)	0.463 840(51)	143.1308(31)	1.5849(28)	-0.0153(43)
1	29 917.7011(30)	0.459 941(36)	142.9939(26)	1.6086(22)	-0.0749(30)
2	30 354.9564(88)	0.456 57(25)	142.8457(66)	1.6332(53)	-0.1174(99)
3	30 792.7596(82)	0.452 00(22)	142.7160(65)	1.6490(52)	-0.1858(96)
4	31 230.416(10)	0.447 70(30)	142.5224(69)	1.6430(61)	-0.2321(95)
5	31 667.3691(92)	0.444 72(35)	142.3772(80)	1.6964(58)	-0.341(13)
6	32 103.1053(76)	0.440 18(24)	142.1860(52)	1.7255(45)	-0.4271(78)
7 ^b	32 537.098(19)	0.435 90(77)	141.983(18)	1.768(12)	-0.562(12)
8 ^b	32 968.900(15)	0.431 49(48)	141.700(16)	1.802(11)	-0.652(29)
9 ^c	33 395.935(25)	0.427 49(71)	-	-	-

^aFigures in parentheses are one standard deviation in units of the last quoted decimal place.

^bMolecular constants were obtained by fitting line positions in both $(v',0)$ and $(v',1)$ bands. The constants determined by Yamada *et al.* (Ref. 32) were used for $Xv''=1$, after being corrected as described in the text.

^cOnly transitions to the $\Omega'=1$ component were included.

precision required to best make use of the short ($1-2\text{ cm}^{-1}$) continuous scan range of the OPO system in investigating the hyperfine structure in the A state. In addition the low-resolution study has made it possible to follow the anomalous trend in the $\Delta G(v+1/2)$ values over a larger range of vibrational levels, and allows the trends in fine structure constants to be considered for the first time. The vibrational spacings plotted in Fig. 5 show quite clearly that the unusual vibrational structure observed for low v , with vibrational spacing initially increasing with v , is common to all three spin-orbit components. This would normally be attributed to the interaction with another electronic state, but there is no state in this region capable of perturbing all three spin-orbit components. It is therefore suggested that the unusual vibrational behavior is solely due to the nature of the A state potential. Figure 5 also shows a small perturbation affecting a single spin-orbit component of $v=4$, for which the $\Omega=2$ component is slightly displaced. This suggests a weak mixing with the $a^1\Delta$ state as this is the only other state in this region with an $\Omega=2$ component.

Application of the noncrossing rule suggests that all three spin-orbit components of the A state correlate with ground state atomic fragments, implying that the spin-orbit splitting should tend to zero at large r . The observation that A (see Table I) is almost invariant over $v=0-8$ can be easily explained by considering the relatively small change in $\langle r \rangle$

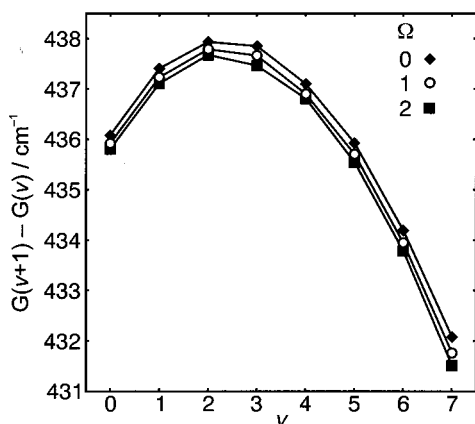


FIG. 5. Separation between successive vibrational levels of the $A^3\Pi$ state.

over this range, from 1.76 \AA for $v=0$ to 1.87 \AA for $v=8$ (see Fig. 12). Preliminary *ab initio* calculations have also shown that the diagonal spin-orbit matrix elements do not vary significantly between 1.3 and 2.1 \AA . In contrast the Λ doubling in the A state steadily increases with v , as can also be seen from Table I. Since both the $\Omega=0^+$ and 0^- components are expected to correlate to the same atomic asymptote, $P(^4S)+F(^2P)$, this v dependence can be associated with an increasing interaction with a Σ state. The obvious candidate is the $b^1\Sigma^+$ state which correlates diabatically with the $P(^2D)+F(^2P)$ limit and is therefore expected to cross (or undergo an avoided crossing with) the A state potential. Such an interaction could significantly perturb the structure of transitions to higher lying vibrational levels.

B. The $d-a$ band system

In the region studied, a progression in the $d^1\Pi-a^1\Delta(v',0)$ system was easily assigned for $v'=0-4$ based on Ref. 16. Figure 6 shows a typical example of the $d-a(0,0)$

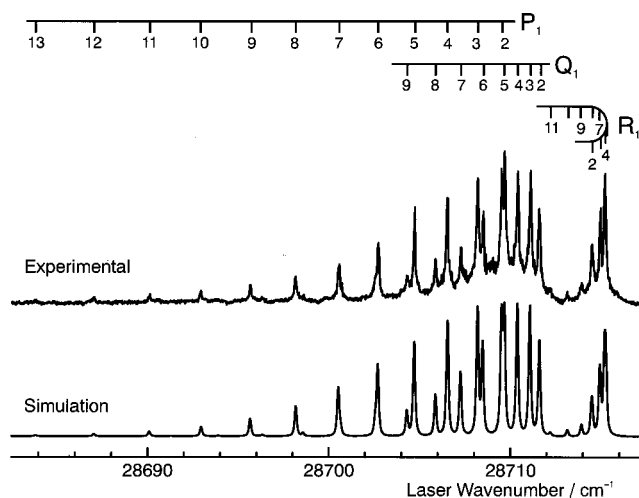


FIG. 6. A rotationally resolved spectrum of the $d^1\Pi-a^1\Delta(0,0)$ band. The upper trace shows experimental data. The lower trace is a simulation generated from the constants given in Table II. The combs above the spectrum are labeled by lower state J . The linewidth of the simulation is a Voigt profile with a Gaussian component of 0.08 cm^{-1} and a Lorentzian component of 0.1 cm^{-1} .

TABLE II. Rotational constants for the $a^1\Delta$ and $d^1\Pi$ states of PF.^a

	Origin ^b /cm ⁻¹	B /cm ⁻¹
$a^1\Delta v=0$	-	0.567 62(16)
$d^1\Pi v=0$	28 712.1124(71)	0.480 89(18)
$d^1\Pi v=1$	29 125.2479(71)	0.474 91(18)
$d^1\Pi v=2$	29 541.8962(65)	0.468 96(19)
$d^1\Pi v=3$	29 960.8212(68)	0.463 90(20)
$d^1\Pi v=4$	30 381.149(11)	0.459 18(28)

^aFigures in parentheses are one standard deviation in units of the last quoted decimal place.

^bTerm values relative to $v=0$ of the $a^1\Delta$ state.

band. There appeared to be no significant decrease in fluorescence intensity with increasing v' , but we were not able to assign any vibrational levels above $v'=4$. An additional band was observed at 30 805 cm⁻¹, close to the expected energy of the $d-a$ (5,0) band, but the rotational structure appeared radically different to that of the other bands and was therefore not assigned to the d state. The rotational line positions in the five observed $d-a$ bands were fitted simultaneously, using a Hamiltonian with a single $B\hat{N}^2$ term to represent each upper and lower state level. Initially the lower state rotational constant was held fixed at the value measured by Douglas and Frackowiak¹⁶ ($B''=0.5676$ cm⁻¹) but a better fit could be obtained by floating B'' and determining an improved value of this parameter.

Table II contains the improved molecular constants for the $d-a$ system, including the first values for $v'=4$. Higher vibrational levels may well predissociate to ground state atomic fragments; the presence of the $P(^4S)+F(^2P)$ dissociation limit between $v=4$ and 5 of the d state is entirely consistent with the D_0 value of $37\,100\pm 3500$ cm⁻¹ determined by Berkowitz *et al.*³³ Figure 7 shows that the vibrational spacing in the $d^1\Pi$ state increases in an even more pronounced fashion with v than that in the $A^3\Pi$ state. As the two states arise from the same configuration, the d state potential may also be unusual. In this case, however, interactions with other electronic states, such as high levels of the A state, could also give this effect.

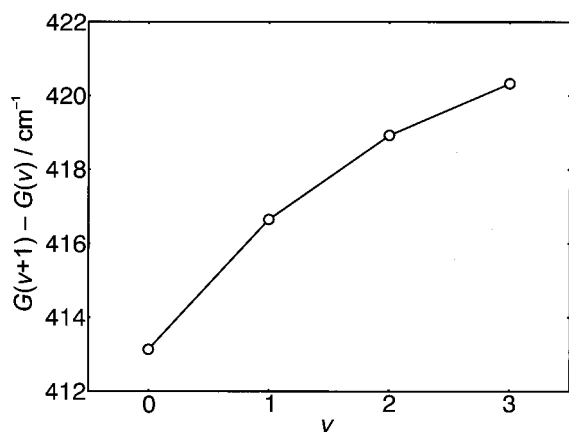
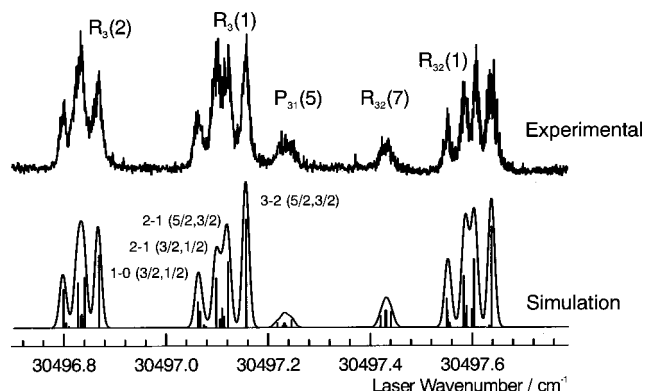
FIG. 7. Separation between successive vibrational levels of the $d^1\Pi$ state.

FIG. 8. A section of the $A^3\Pi_2-X^3\Sigma^-(2,0)$ sub-band, showing the observed and calculated spectrum of one P branch and four R branch transitions, including the associated hyperfine structure. These transitions are labeled in the upper experimental trace by lower state J . The labels describing the hyperfine structure in the $R_3(1)$ transition represent $F'-F''$ and $(F'_1-F''_1)$, where the quantum numbers F and F_1 are as defined in the text. The simulation shows a stick spectrum calculated using the constants given in Table III, and the convolution of this with an instrumental Gaussian function with FWHM 0.015 cm⁻¹.

IV. HYPERFINE RESOLUTION STUDY OF THE $A-X$ BAND SYSTEM

High-resolution spectra of the $A^3\Pi-X^3\Sigma^-(v',0)$ bands have been recorded for $v'=2-3$ and $v'=5-7$. Figures 8 and 9 show typical spectra from the (2,0) and (6,0) bands, respectively. Spectra of the $^3\Pi_2$ components showed a clear hyperfine splitting for some branches (Fig. 8) and some of the low J lines for the $^3\Pi_1$ component showed clear broadening and asymmetry (Fig. 9). The overall linewidth obtained in these studies was ~ 0.015 cm⁻¹ which is entirely consistent with a contribution of ~ 0.006 cm⁻¹ from frequency doubling the output from the OPO and 0.011 cm⁻¹ from a residual Doppler width at 10 K.

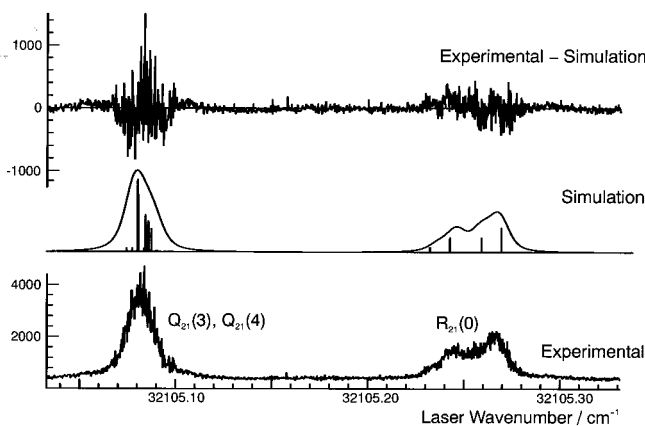


FIG. 9. Two rotational transitions in the $A^3\Pi_1-X^3\Sigma^-(6,0)$ spectrum. The shape of the higher energy peak, $R_{21}(0)$, is influenced by the underlying unresolved hyperfine structure due to nuclear spin-orbit coupling. The peaks to lower energy, $Q_{21}(3)$ and $Q_{21}(4)$, are not broadened and their widths are determined by the OPO bandwidth. The linewidth determined from the contour fitting process was a Voigt profile with a Gaussian component of 0.01 cm⁻¹ and a Lorentzian component of 0.005 cm⁻¹. The upper trace shows the residuals from the line contour fitting process.

TABLE III. Rotational and hyperfine constants for the $A^3\Pi$ state of PF.^a

v'	2	3	5	6	7
Origin/cm ⁻¹	30 354.939 44(48)	30 792.708 42(72)	31 667.302 65(44)	32 103.039 95(75)	32 537.049 91(56)
B /cm ⁻¹	0.456 404(24)	0.452 361(42)	0.444 225(29)	0.440 105(75)	0.435 930(35)
D /cm ⁻¹	$1.85(19) \times 10^{-6}$	$1.34(34) \times 10^{-6}$	$1.53(31) \times 10^{-6}$	$1.19(21) \times 10^{-6}$	$8.5(37) \times 10^{-7}$
A /cm ⁻¹	142.843 69(42)	142.703 37(54)	142.374 65(26)	142.192 02(46)	141.969 73(32)
λ /cm ⁻¹	1.615 19(38)	1.645 44(68)	1.700 63(28)	1.737 90(43)	1.782 36(35)
o /cm ⁻¹	-0.121 12(81)	-0.178 4(10)	-0.325 31(29)	-0.426 17(69)	-0.562 07(38)
a (P) ^b /cm ⁻¹	0.029 0(17)	0.029 0(30)	0.027 1(13)	0.026 3(22)	0.027 3(28)
$b_F + \frac{2}{3}c$ (P)/cm ⁻¹	0.018 9(56)	0.023 6(20)	0.025 6(17)	0.024 2(28)	0.025 7(57)
a (F) ^b /cm ⁻¹	0.017 5(14)	0.021 3(42)	0.017 5(14)	0.021 0(13)	0.017 2(24)
$b_F + \frac{2}{3}c$ (F)/cm ⁻¹	0.030 5(57)	0.023 5(21)	0.021 9(20)	0.021 5(28)	0.021 2(51)

^aFigures in parentheses are one standard deviation in units of the last quoted decimal place.

^bDetermined from contour fit.

The spectra obtained from the OPO system were analyzed using a Hamiltonian of the form

$$\hat{H}_{\text{tot}} = \hat{H}_{\text{rot}} + \hat{H}_{\text{hyp}}(\text{P}) + \hat{H}_{\text{hyp}}(\text{F}), \quad (2)$$

where the Hamiltonian excluding the effects of nuclear spin, \hat{H}_{rot} , is given by Eq. (1). The hyperfine parts take the same standard form³⁴ for both nuclei

$$\hat{H}_{\text{hyp}} = a\hat{I}_z\hat{L}_z + b_F\hat{\mathbf{I}}\cdot\hat{\mathbf{S}} + \frac{1}{3}c(3\hat{I}_z\hat{S}_z - \hat{\mathbf{I}}\cdot\hat{\mathbf{S}}), \quad (3)$$

with $\hat{\mathbf{I}}$ being the spin of the phosphorus or fluorine nucleus as required. The energy levels were calculated by setting up the Hamiltonian matrix in a Hund's case (a_β) basis using the coupling scheme

$$\hat{\mathbf{F}}_1 = \hat{\mathbf{J}} + \hat{\mathbf{I}}_P; \quad \hat{\mathbf{F}} = \hat{\mathbf{F}}_1 + \hat{\mathbf{I}}_F, \quad (4)$$

and including all possible F_1 , J and Ω for a given F and parity in the basis. As the hyperfine constants for both nuclei are similar in magnitude, F_1 is not expected to be a good quantum number, so diagonalization of the full matrix is important. However, inspection of the coefficients from this indicates that F_1 is good enough to use as a label for all except $A^3\Pi_0$ levels, though the fitting process does not rely on this. Transition intensities are calculated by transforming the matrix elements of the dipole moment in the Hund's case (a_β) basis using the coefficients from the diagonalization.

As the $A^3\Pi$ state is essentially pure Hund's case (a) there are some limitations on the hyperfine parameters that can be determined; this can be seen by rearranging the hyperfine Hamiltonian [Eq. (3)] to:

$$\begin{aligned} \hat{H}_{\text{hyp}} &= \{a\hat{L}_z + (b_F + \frac{2}{3}c)\hat{S}_z\}\hat{I}_z + \frac{1}{2}(b_F - \frac{1}{3}c)(\hat{I}_+\hat{S}_- + \hat{I}_-\hat{S}_+) \\ &\approx \{a\Lambda + (b_F + \frac{2}{3}c)\Sigma\}\hat{I}_z. \end{aligned} \quad (5)$$

The second step follows because the $\hat{I}_\pm\hat{S}_\mp$ term mixes the widely separated spin-orbit components of the Π state and thus only shifts the energy levels by a few MHz which is below our experimental precision. Equation (5) shows that the hyperfine structure in the $^3\Pi_1$ component (where $\Sigma=0$) is purely determined by the nuclear spin-orbit coupling constant a . The splittings in the $\Omega=0$ and 2 components are governed by $a \pm (b_F + \frac{2}{3}c)$ giving two determinable combinations for each nucleus, a and $b_F + \frac{2}{3}c$.

The only independent information on a thus comes from the poorly resolved hyperfine structure in the $\Omega=1$ components (Fig. 9). A line contour fitting process was therefore used to extract the a constant for both nuclei as described in detail previously.³⁵ This used line intensities calculated as described above with the line shape modeled with an empirical combination of Gaussian and Lorentzian components. At least five separate scans were fit for each vibrational level. The results given in Table III are an average of these, with a standard deviation estimated from the scatter in these measurements. The fitted scans included one sharp line and one hyperfine broadened line so the instrument function (typically 0.015 cm^{-1} full width half maximum) is determined from the sharp lines, leaving a for each nucleus to be determined from the excess width and asymmetry of the other lines. In a few cases there were two fits with different values for the parameters that gave equally good agreement with the experimental data. In these cases one of the fits gave a negative value for a for one of the nuclei which was rejected as being unphysical based on the interpretation discussed below. All the other constants, including $(b_F + \frac{2}{3}c)$, were obtained by conventional line position fits with the nuclear spin-orbit coupling constants fixed at the value determined by the contour fit. All of the lines observed for a particular vibronic band were included in the line position fits, though some of the broader lines were given a reduced weight. The combination $(b_F + \frac{2}{3}c)$ for each nucleus, as determined from this fit, along with the other molecular constants are given in Table III. Comparison of these constants with those obtained in the low-resolution study show excellent agreement in all cases.

V. HYPERFINE RESOLUTION STUDY OF THE $d-a$ BAND SYSTEM

Spectra of the $d^1\Pi - a^1\Delta$ (4,0) band were also taken at high-resolution. A few of the low J rotational lines showed clear broadening or partially resolved hyperfine structure, as can be seen in Fig. 10. Equation (5) also applies here, and can be simplified even further as $\Sigma=0$, yielding:

$$\hat{H}_{\text{hyp}} = a\Lambda\hat{I}_z \quad (6)$$

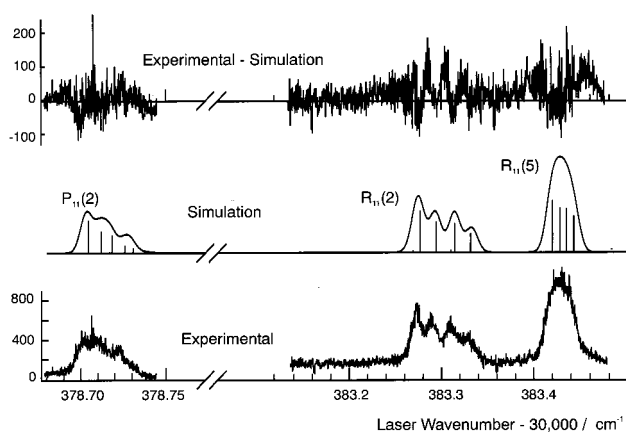


FIG. 10. Three rotational lines from the $d^1\Pi-a^1\Delta(4,0)$ band showing clear hyperfine broadenings due to the nuclear spin-orbit coupling. The linewidth determined from the contour fitting process was an instrumental Gaussian function FWHM of 0.015 cm^{-1} . The upper trace shows the residuals from the line contour fitting process.

so only one hyperfine constant is required for each nucleus. The additional complication here is the lack of hyperfine information for the lower state, as a microwave spectrum is not available. Fortunately the splittings in the two lowest J'' transitions [$R_1(2)$ and $P_1(2)$] have a sufficiently different dependence on the upper and lower state hyperfine constants to allow both to be determined. A contour fit was therefore undertaken using $R_1(2)$ and $P_1(2)$, with $R_1(5)$ included to determine the linewidth. Five separate scans were fitted and the nuclear spin-orbit coupling constants for both nuclei were determined for both the $d^1\Pi$ and the $a^1\Delta$ states; these are given in Table V.

VI. HYPERFINE STRUCTURE INTERPRETATION

To interpret the nuclear spin-orbit coupling constant, the definition provided by Kristiansen and Veseth³⁶ is perhaps the most helpful

$$a = 2g_N\mu_B\mu_N \frac{1}{\Lambda} \left\langle \eta\Lambda S\Sigma \left| \sum_i \frac{\hat{I}_{iz}}{r_i^3} \right| \eta\Lambda S\Sigma \right\rangle. \quad (7)$$

Among other things this implies that the sign of a will be solely determined from the sign of g_N , and should therefore be positive for both P and F. This is used to reject any negative values for a returned by the line contour fitting process. Considering the $\dots 7\sigma^2 2\pi^4 3\pi 8\sigma$ configuration expected for

TABLE V. Hyperfine and rotational constants for the $a^1\Delta$ and the $d^1\Pi$ states of PF.^a

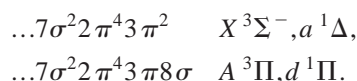
	$a^1\Delta v''=0$	$d^1\Pi v'=4$
B/cm^{-1}	0.567 58(27)	0.458 90(24)
Origin/ cm^{-1}	0.0	30 381.1918(22)
$a(\text{P})^b/\text{cm}^{-1}$	0.026 3(39)	0.0219(14)
$a(\text{F})^b/\text{cm}^{-1}$	0.014 36(39)	0.012 53(78)

^aFigures in parentheses are one standard deviation in units of the last quoted decimal place.

^bDetermined from contour fit.

the A state, measurement of a in the upper state should allow the determination of the spatial average $\langle 3\pi|r^{-3}|3\pi\rangle$. Using atomic values of $\langle r^{-3}\rangle$ as tabulated by Morton and Preston,³⁷ the spin density in the 3π orbital on each atom can be estimated for each vibrational level. *Ab initio* calculations indicate only moderate dipole moments (0.89 D in the $X^3\Sigma^-$ state²³ and 0.70 D in the $a^1\Delta$ state²⁴) so neutral atoms are used as a basis, rather than ions. The derived spin densities are given in Table IV and are plotted in Fig. 11 along with the total spin density, which is consistently 100% within the uncertainty arising from a . The same approach can be used for the a values for the $d^1\Pi$ and $a^1\Delta$ states, and the corresponding spin densities are also included in Table IV.

It is striking that the π spin densities are essentially the same for all the states studied, including the ground state. (The spin density for the ground state is as determined from c by Saito *et al.*²²) However, this is consistent with the simple molecular orbital picture for each state:



In each case the unpaired π electron density is in the 3π orbital, and the observed values confirm both the above molecular orbital picture, and that the molecular orbitals do not change significantly between the different electronic states. The 3π anti-bonding orbital is essentially localized on the phosphorus, which is consistent with the large difference in electronegativities. In this light the moderate dipole moments given by *ab initio* calculations are perhaps surprising and indicate smaller polarization in the fully occupied orbitals. It would be interesting to compare with *ab initio* calculations of a but these are unfortunately not available for the values measured here.

TABLE IV. Values derived from the hyperfine constants in PF.

	$X^3\Sigma^- v''=0^a$	$a^1\Delta v''=0$	$A^3\Pi v'=2$	$A^3\Pi v'=3$	$A^3\Pi v'=5$	$A^3\Pi v'=6$	$A^3\Pi v'=7$	$d^1\Pi v'=4$
$b_F(\text{P})/\text{cm}^{-1}$	0.003 90	-	0.0131	0.0178	0.0202	0.0189	0.0202	-
$b_F(\text{F})/\text{cm}^{-1}$	0.002 98	-	0.0270	0.0192	0.0184	0.0173	0.0178	-
$c(\text{P})/\text{cm}^{-1}$	-0.0168	-	0.0087	0.0087	0.0081	0.0079	0.0082	-
$c(\text{F})/\text{cm}^{-1}$	-0.008 02	-	0.0053	0.0064	0.0053	0.0063	0.0052	-
(3π) spin density (P)	91.3%	86%	95%	95%	89%	86%	89%	72%
(3π) spin density (F)	9.1%	10%	12%	15%	12%	15%	12%	9%
s character (P)	0.88%	-	3.0%	4.0%	4.5%	4.3%	4.6%	-
s character (F)	0.17%	-	1.5%	1.1%	1.0%	1.0%	1.0%	-
Calculated A/cm^{-1}	-	-	146.5	149.9	137.9	137.5	138.5	-

^a b_F and c measured directly by Saito *et al.* (Ref. 22).

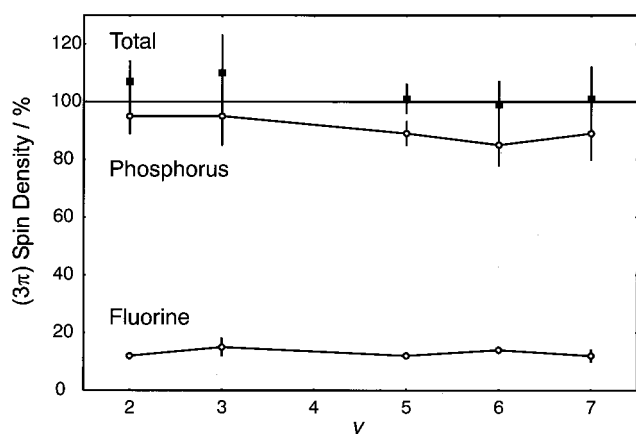


FIG. 11. (3π) spin densities on each atom. The error bars are estimated from the standard deviations of the fitted nuclear-spin-orbit constants in Table III. The filled squares represent the total (3π) spin density.

In principle, the same information on spin densities is available from the (electron) spin-orbit coupling constant, A , as detailed in Sec. 4.3.1 of Lefebvre-Brion and Field.³⁸ Values of A predicted using our π spin densities are included in Table IV. These are in good agreement with the observed values, though as detailed in Ref. 39, the atomic values are so similar the predictions are essentially independent of the spin distribution.

Although only the combination $(b_F + \frac{2}{3}c)$ can be determined directly from the experimental data, these values can be used in conjunction with the nuclear spin-orbit coupling constants to obtain further insight into the nature of the electronic wave function. The simple MO picture would predict no s character in the wave function, suggesting $b_F = 0$. Calculating c and then spin densities with this assumption gives totally unreasonable spin densities ($\sim 400\%$ on P) demonstrating that it is not possible to ignore b_F . However, it has been found for a number of molecules containing a single unpaired electron that spin densities can be determined from the dipole-dipole term

$$c = \frac{3}{2} g_s g_N \mu_B \mu_N \bar{\Sigma} \left\langle \eta \Lambda S \Sigma \left| \sum_i \frac{(3 \cos^2 \theta_i - 1) \hat{s}_{iz}}{r_i^3} \right| \eta \Lambda S \Sigma \right\rangle \quad (8)$$

with the assumption that the angular part of the integral can be evaluated using hydrogenic p orbitals⁴⁰ about the nucleus under consideration. For a $p\pi$ orbital this angular integral is $-2/5$, and is $4/5$ for a $p\sigma$ orbital.³⁹ For the A state, with a $p\pi$ $p\sigma$ configuration, this factor is the average of the 2, i.e., $1/5$. We can thus estimate c from a and then derive b_F from the experimentally measured value of $(b_F + \frac{2}{3}c)$. If the same distribution of the unpaired electron between P and F in the $p\sigma$ and $p\pi$ orbitals is assumed (it is unlikely to be less polarized in the $p\sigma$ than the $p\pi$) then

$$c = \frac{3g_s}{20} a. \quad (9)$$

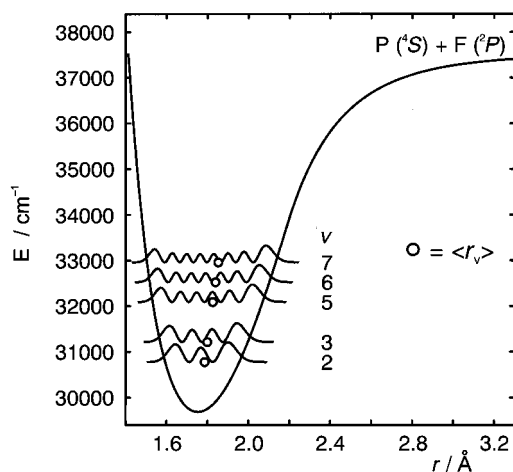


FIG. 12. Potential energy curve for the $A^3\Pi$ state. The square of the vibrational wave function, and the radial expectation value $\langle r \rangle_v$, are plotted for each level in which the hyperfine constants have been determined.

The values derived for c and b_F using the above procedure are given in Table IV. Also tabulated is the s character of the orbitals containing the unpaired electrons determined by comparing b_F to the expectation values of the atomic wave functions at the nucleus.³⁷ It is difficult to estimate the errors introduced in the determination of b_F , but it is likely that the differences in the s character across the range of vibrational levels investigated are not statistically significant. Even with this apparent uncertainty, it is clear that the s character of the orbitals containing the unpaired electrons is larger in the A state (the average being P: 4.1%, F: 1.1%) than in the ground state (P: 0.88%, F: 0.17%). This difference can be explained by considering the orbitals involved; in the ground state, the unpaired electrons are in the $p\pi$ orbitals, which have the wrong symmetry for mixing with an s orbital, and the small s character that is present is normally explained by invoking spin polarization.⁴⁰ In the A state one of the unpaired electrons occupies a $p\sigma$ orbital, and mixing with an s orbital is then symmetry allowed. The mixing, however, is still small, implying that the simple molecular orbital picture only requires a small adjustment to account for sp hybridization.

As a result of the relatively small range of vibrational levels investigated, and the uncertainties in the determination of the nuclear spin-orbit constants, it is difficult to confirm a vibrational dependence to the spin densities on the basis of Fig. 11. Figure 12 shows the A state potential with the square of the vibrational wave function and the radial expectation value for each vibrational level for which hyperfine constants were determined. Note that the variation in $\langle r \rangle_v$ between $v' = 2-7$ is actually quite small ($1.79-1.85 \text{ \AA}$) and accounts for the small variation in the hyperfine parameters and the spin densities and s characters derived from them. Higher vibrational levels should show more dramatic changes as, for example, the $a\hat{I}_z\hat{L}_z$ interaction for the phosphorus atom should go zero at the dissociation limit as the atom has no electron orbital angular momentum. We could not study higher vibrational levels here because of poor Franck-Condon factors for transitions to $v' > 9$ from $v'' = 0$. However, reasonably straightforward modifications to the meth-

ods used here, such as a PF source with a higher vibrational temperature or a double resonance scheme, could probe these interesting higher vibrational levels.

VII. CONCLUSIONS

The range of rotationally analyzed levels in the $A^3\Pi$ state of PF has been extended up to $v'=9$ confirming the anomalous trend in the $\Delta G(v+1/2)$ values, and extending the range of rotational analysis. The $d^1\Pi-a^1\Delta$ system has also been investigated at low-resolution, and the observation of the fifth vibrational level is reported here for the first time.

Building on the low-resolution analysis, the high-resolution OPO system has provided the opportunity of taking sub-Doppler spectra of the $A^3\Pi-X^3\Sigma^-$ and $d^1\Pi-a^1\Delta$ systems which have revealed significant hyperfine splittings in both systems. Analysis of the hyperfine structure for all the electronic states involved has provided valuable insight into the electronic wave functions, including an estimation of spin density and s character at each nucleus. It would be very interesting to extend the range of vibrational levels studied, and one of the benefits of the system described here is that the application of double resonance methods only requires the addition of a conventional pulsed laser rather than a second high-resolution source.

The study of hyperfine structure in the A state of PF has proved an excellent demonstration of the potential of the injection seeded OPO system. Such an all solid-state system which provides broadly tuneable, narrow bandwidth light from the near infrared to the UV will undoubtedly be an invaluable addition to many laboratories, with applications extending far beyond the high-resolution spectroscopy shown here.

ACKNOWLEDGMENTS

The authors would like to gratefully acknowledge EPSRC for project funding, an advanced fellowship (S.H.A.), a post-doctoral fellowship (O.V.C.) and two Ph. D. studentships (J.A.J.F. and J.M.F.E.). We also gratefully acknowledge Spectra-Physics for financial and technical support, and Keith Rosser for his expert advice on the construction of the injection seeded OPO system.

¹C. M. Western, W. S. Barney, S. G. Clement, T. J. Slotterback, and K. C. Janda, *Z. Phys. D: At., Mol. Clusters* **36**, 273 (1996).

²W. S. Barney, C. M. Western, and K. C. Janda, *J. Chem. Phys.* **113**, 7211 (2000).

³D. W. Pratt, *Annu. Rev. Phys. Chem.* **4**, 481 (1998).

⁴R. N. Dixon, J. Nightingale, C. M. Western, and X. Yang, *Chem. Phys. Lett.* **151**, 328 (1988).

⁵S. H. Ashworth, J. M. F. Elks, and C. M. Western, *Chem. Phys. Lett.* **328**, 197 (2000).

⁶J. E. Bjorkholm and H. G. Danielmeyer, *Appl. Phys. Lett.* **15**, 171 (1969).

⁷B. A. Richman, K. W. Aniolek, T. J. Kulp, and S. E. Bisson, *J. Opt. Soc. Am. B* **17**, 1233 (2000).

⁸S. Wu, V. A. Kapinus, and G. A. Blake, *Opt. Commun.* **159**, 74 (1999).

⁹Y. X. Fan, R. C. Eckardt, R. L. Byer, J. Nolting, and R. Wallenstein, *Appl. Phys. Lett.* **53**, 2014 (1988).

¹⁰A. Fix, T. Schroder, R. Wallenstein, J. G. Haub, M. J. Johnson, and B. J. Orr, *J. Opt. Soc. Am. B* **10**, 1744 (1993).

¹¹J. G. Haub, M. J. Johnson, B. J. Orr, and R. Wallenstein, *Appl. Phys. Lett.* **58**, 1718 (1991).

¹²O. Votava, J. R. Fair, D. F. Plusquellic, E. Riedle, and D. J. Nesbitt, *J. Chem. Phys.* **107**, 8854 (1997), and references therein.

¹³M. J. T. Milton, T. D. Gardiner, G. Chourdakis, and P. T. Woods, *Opt. Lett.* **19**, 281 (1994).

¹⁴G. W. Baxter, Y. He, and B. J. Orr, *Appl. Phys. B: Lasers Opt.* **67**, 753 (1998).

¹⁵P. Bourdon, M. Pealat, and V. I. Fabelinsky, *Opt. Lett.* **20**, 474 (1995).

¹⁶A. E. Douglas and M. Frackowiak, *Can. J. Phys.* **40**, 832 (1962).

¹⁷I. Kovács, *Can. J. Phys.* **42**, 2180 (1964).

¹⁸U. K. Roychowdhury, S. Naxakis, J. A. Coxon, D. S. Richards, D. Z. Cao, and D. W. Setser, *Chem. Phys.* **118**, 427 (1987).

¹⁹J. M. F. Elks and C. M. Western, *J. Chem. Phys.* **110**, 7699 (1999).

²⁰J. Xu, D. W. Setser, and R. Hamman, *J. Phys. Chem.* **99**, 3173 (1995).

²¹B. Nizamov and D. W. Setser, *J. Mol. Spectrosc.* **206**, 53 (2001).

²²S. Saito, Y. Endo, and E. Hirota, *J. Chem. Phys.* **82**, 2947 (1985).

²³G. de Brouckère, *Chem. Phys.* **262**, 229 (2000).

²⁴G. de Brouckère, *Chem. Phys.* **264**, 163 (2001).

²⁵R. Colin, J. Devillers, and F. Prevot, *J. Mol. Spectrosc.* **44**, 230 (1972).

²⁶L. Latifzadeh and K. Balasubramanian, *Chem. Phys. Lett.* **243**, 243 (1995).

²⁷J. D. Howe, M. N. R. Ashfold, C. M. Western, and J. W. Hudgens, *J. Chem. Phys.* **104**, 2789 (1996).

²⁸W. R. Bosenberg, W. S. Pelouch and C. L. Tang, *Appl. Phys. Lett.* **55**, 1952 (1989).

²⁹D. C. Hovde, J. H. Timmermans, G. Scoles, and K. K. Lehmann, *Opt. Commun.* **86**, 294 (1991).

³⁰K. N. Rosser, Q.-Y. Wang, and C. M. Western, *J. Chem. Soc., Faraday Trans.* **89**, 391 (1993).

³¹T. J. Slotterback, S. G. Clement, K. C. Janda, and C. M. Western, *J. Chem. Phys.* **103**, 9125 (1995).

³²C. Yamada, M. C. Chang, and E. Hirota, *J. Chem. Phys.* **86**, 3804 (1987).

³³J. Berkowitz, J. P. Greene, J. Foropoulos, Jr., and O. M. Nesković, *J. Chem. Phys.* **81**, 6166 (1984).

³⁴R. A. Frosch and H. M. Foley, *Phys. Rev.* **88**, 1337 (1952).

³⁵T. J. Slotterback, S. G. Clement, K. C. Janda, and C. M. Western, *J. Chem. Phys.* **101**, 7221 (1994).

³⁶P. Kristiansen and L. Veseth, *J. Chem. Phys.* **84**, 2711 (1986).

³⁷J. R. Morton and K. F. Preston, *J. Magn. Reson.* (1969-1992) **30**, 577 (1978).

³⁸H. Lefebvre-Brion and R. W. Field, *Perturbations in the Spectra of Diatomic Molecules* (Academic, Orlando, 1986).

³⁹J. M. F. Elks, Ph. D. thesis, University of Bristol (2001).

⁴⁰E. Hirota, *High Resolution Spectroscopy of Transient Species* (Springer-Verlag, Berlin, 1985).